Monthly Notices of the ROYAL ASTRONOMICAL SOCIETY

MNRAS **524,** 3582–3595 (2023) https://doi.org/10.1093/mnras/stad2133
Advance Access publication 2023 July 17

T Tauri stars in the SuperWASP and NSVS surveys II. Spectral modelling

L'. Hambálek [1]★ V. Krushevska,[1] T. Pribulla [1] M. Vaňko,[1] J. Budaj,[1] M. Fiorucci,[2] Z. Garai [1,3,4] E. Guenther [5] R. Komžík,[1] E. Kundra,[1] U. Munari[6] and B. Smalley [7]

[1]*Astronomical Institute, Slovak Academy of Sciences, Tatranská Lomnica, 05960 Tatranská Lomnica, Slovakia*
[2]*ANS Collaboration, Astronomical Observatory, Via Osservatorio Astrofisico, I-36012 Asiago (VI), Italy*
[3]*MTA-ELTE Exoplanet Research Group, Szent Imre h. u. 112, H-9700 Szombathely, Szent Imre h. u. 112, Hungary*
[4]*ELTE Gothard Astrophysical Observatory, Szent Imre h. u. 112, H-9700 Szombathely, Szent Imre h. u. 112, Hungary*
[5]*Thüringer Landessternwarte, Sternwarte 5, G-077 78 Tautenburg, Germany*
[6]*INAF Astronomical Observatory of Padova, Via Osservatorio Astrofisico, I-36012 Asiago (VI), Italy*
[7]*Astrophysics Group, Keele University, Keele Rd, Keele ST5 5BG, UK*

Accepted 2023 July 13. Received 2023 July 10; in original form 2023 April 17

ABSTRACT

We present results from long-term spectroscopic monitoring of 21 T-Tauri stars located in the Taurus–Auriga star-forming region (SFR). We combine medium and high-dispersion Echelle spectroscopy obtained at the Stará Lesná, Skalnaté Pleso (both in Slovakia), and Tautenburg (Germany) observatories with low-resolution flux-calibrated spectra from Asiago (Italy) observatory all taken between 2015 and 2018. We extend the coverage by additional medium-resolution spectra from Stará Lesná obtained in 2022. In the previous paper, we measured photometric periods of these targets in a range of 0.7–3.1 d, which could be due to the rotation of a spotted surface or binarity. Here, we use the broadening-function technique to determine the radial and projected rotational velocities to reveal any close binary companion. Our analysis concludes that no such companion is present with an orbital period equal to the photometric period. We focus our analysis primarily on determining atmospheric parameters such as surface gravity $\log g$, effective temperature $T_{\rm eff}$, and metallicity [Fe/H]. Additionally, we measure the equivalent width of H α, Li I, and interstellar Na I lines. We also investigate the effect of possible reddening on individual targets and construct the HR diagram of our sample. Using pre-main-sequence evolutionary models, we determine the age of our targets. This analysis hints at ages younger than 50 Myr with mean age 5 ± 3 Myr, masses between 0.75 and 2.10 $M_\odot$, and minimum radii in the range 0.60–3.17 $R_\odot$. Altogether, the results are consistent with expected young stars with larger radii than those of main-sequence stars.

Key words: stars: variables: T Tauri, Herbig Ae/Be.

1 INTRODUCTION

Understanding the properties of T Tauri stars (TTSs) is an utmost priority to comprehend the evolution of Solar-type stellar objects, and also the formation and evolution of extrasolar planets. Effective temperature ($T_{\rm eff}$), surface gravity ($\log g$), and metallicity ([Fe/H]) are fundamental atmospheric parameters. The effective temperature and the surface gravity are important since the two parameters determine the position of the object on the HR diagram, and are related to age and mass.

According to the equivalent width (EW) of the H α line, the TTSs can be classified into classical T Tauri-type stars (abbreviated as CTTS) and T Tauri-type stars with weak emission lines (i.e. weak-line T Tauri-type stars, abbreviated as WTTS) (see e.g. Martin 1997; White & Basri 2003; Xing 2010).

TTSs possess conspicuous absorption lines of lithium and exhibit very intense chromospheric activities (Herbig 1962). Because of accreting mass from their discs via magnetospheric accretion, they feature large ultraviolet excesses (Ingleby et al. 2011), some are associated with P Cygni profiles (Symington, Harries & Kurosawa 2005; Kurosawa, Romanova & Harries 2011), veiling (Basri & Batalha 1990; Hartigan, Edwards & Ghandour 1995), and infrared excess (Hartmann, Herczeg & Calvet 2016; Manzo-Martínez et al. 2020). All this implies that for the TTSs with weak emission lines, the accretion discs around the stars have partially or even completely vanished. We have to note that many candidates for pre-main sequence (PMS) stars have been singled out in X-ray surveys, on the basis of their strong X-ray emission, and then confirmed to be weak-line TTSs on the basis of their high lithium content, as well as lack of UV and IR excess (e.g. Neuhäuser 1997; Feigelson & Montmerle 1999; Walter et al. 2000).

For late-type stars, the abundance of lithium on the stellar surface is generally considered an indicator of age, as lithium is strongly depleted already at the zero-age main sequence (ZAMS). It is, therefore, possible to distinguish between the PMS and ZAMS stars by comparing the lithium abundance with that of a young ZAMS cluster, e.g. the Pleiades (e.g. Neuhaeuser et al. 1997; Sterzik et al. 2005; Xing et al. 2021; Campbell-White et al. 2023). However, it was found that lithium abundances can be model-dependent. Therefore, it seems that a better approach is to compare the EW of the Li I 6708 line instead of the lithium abundances.

Obviously, EW(Li 6708) is very sensitive to the effective temperature of the star, therefore this comparison has to be done in the $T_{\rm eff}-EW$ diagram (see Section 3.1). On the other hand, the H α line is not useful as a PMS indicator because some late-type main

★ E-mail: lhambalek@ta3.sk

Table 1. The basic characteristic of the selected targets. Distances are calculated from parallaxes from the *Gaia* DR3 (Gaia Collaboration et al. 2022) catalogue. Distance of HD 286178 is from TGAS (Michalik, Lindegren & Hobbs 2015). Rotational period $P_{\rm rot}$ was determined by light-curve variability due to spots (see Hambálek et al. 2019). Numbers in parentheses are errors given by the least significant digit.

TTS	Object name	α_{2000} [h m s]	δ_{2000} [° ′ ″]	B [mag]	V [mag]	Sp. type (in lit.)	$P_{\rm rot}$ [d]	Distance [pc]	References
01	HD 285 281	04 00 31.07	19 35 20.8	11.34(7)	10.17(4)	K1/F9	1.1711(37)	$136.22^{+0.43}_{-0.43}$	1, 2, 6, 12
02	V1298 Tau	04 05 19.61	20 09 25.2	11.11(9)	10.12(5)	K1.5	2.8489(8)	$108.02^{+0.23}_{-0.23}$	2, 3, 6, 12
03	HD 284135	04 05 40.58	22 48 12.0	9.99(4)	9.39(3)	G3V	0.8179(58)	–	1, 6
04	HD 284149	04 06 38.80	20 18 11.2	10.21(4)	9.63(3)	G0-1	1.0712(7)	$117.48^{+0.25}_{-0.25}$	1, 2, 4, 6
05	HD 281691	04 09 09.74	29 01 30.3	11.48(9)	10.68(7)	G8III-K2	2.6267(237)	$108.64^{+0.20}_{-0.20}$	1, 6
06	HD 284266	04 15 22.92	20 44 16.9	11.20(11)	10.51(9)	K0V	1.8433(10)	$122.40^{+0.36}_{-0.36}$	1, 2, 6
07	HIP 20782	04 27 05.98	18 12 37.2	9.09(2)	8.73(2)	G5	–	$127.21^{+1.60}_{-1.56}$	11
08	HD 284503	04 30 49.19	21 14 10.7	11.07(8)	10.24(1)	G8	0.7370(3)	$109.67^{+0.27}_{-0.26}$	1, 6
09	HD 284496	04 31 16.86	21 50 25.3	11.59(9)	10.80(6)	K0	2.7738(8)	$124.64^{+0.26}_{-0.26}$	1, 5
10	HD 285840	04 32 42.43	18 55 10.2	9.53(10)	9.38(8)	K1V	1.5463(2)	$89.98^{+0.14}_{-0.14}$	2, 5, 6
11	HD 285957	04 38 39.07	15 46 13.6	11.75(17)	10.86(8)	G6-K1	3.0863(10)	$139.82^{+0.35}_{-0.35}$	2, 5, 6
12	HD 283798	04 41 55.16	26 58 49.4	10.21(3)	9.55(2)	G7	0.9831(2)	$109.93^{+0.21}_{-0.21}$	1, 2, 6
13	HD 283782	04 44 54.40	27 17 45.5	10.69(6)	9.80(4)	K1	2.0181(4)	$205.08^{+8.69}_{-8.01}$	1, 2, 6
14	HD 30171	04 45 51.30	15 55 49.7	10.12(4)	9.36(3)	G3-5	1.1058(33)	$168.19^{+3.46}_{-3.32}$	2, 5, 6
15	HD 31281	04 55 09.62	18 26 31.1	9.83(3)	9.14(2)	G1	0.6771(1)	$121.28^{+0.43}_{-0.43}$	1, 2, 6
16	HD 286179	04 57 00.65	15 17 53.1	10.99(6)	10.39(5)	G3	3.1249(20)	$121.11^{+0.45}_{-0.45}$	5, 6
17	HD 286178	04 57 17.66	15 25 09.5	11.15(4)	10.23(3)	K1	1.7027(6)	$138.11^{+5.55}_{-5.13}$	2, 5, 6
18	HD 283447	04 14 12.92	28 12 12.3	12.07(10)	10.68(10)	K3V	3.0836(210)	$120.10^{+1.92}_{-1.86}$	8, 13
19	HD 283572	04 21 58.85	28 18 06.5	9.80(3)	9.03(2)	G4-5	1.5462(38)	$127.01^{+0.31}_{-0.31}$	1, 2
20	HD 285778	04 27 10.57	17 50 42.6	11.07(7)	10.22(5)	G6/K1	2.8554(17)	$118.89^{+0.30}_{-0.29}$	7
21	HD 283518	04 18 31.12	28 27 16.1	12.13(23)	10.75(7)	K3V	1.8706(14)	$129.36^{+0.36}_{-0.35}$	1, 9, 10

Notes. References: (1) Grankin (2013), (2) Daemgen et al. (2015), (3) Grankin, Artemenko & Melnikov (2007), (4) Bonavita et al. (2014), (5) Bouvier et al. (1997), (6) Wichmann et al. (2000), (7) Grankin et al. (2008), (8) Welty (1995), (9) Stelzer et al. (2003), (10) Fernández et al. (2004), (11) Høg et al. (2000), (12) Kraus et al. (2017), and (13) Kenworthy et al. (2022).

sequence stars have significant H α emission, while in some PMS stars, H α emission may not even fill up the photospheric absorption. This could happen in early K or G stars because photospheric H α absorption depends on the spectral type. Stars without Li absorption display strong chromospheric activity, as indicated by H α in emission above the photospheric continuum, are regarded as likely counterparts of the X-ray source but not as WTTS (Wichmann et al. 1996).

The presented paper is a continuation of our work with the sample (see Table 1), which has been described in Hambálek et al. (2019). We have found many bona fide TTSs, originally designated as members of the nearest known star-forming region (SFR) Taurus–Auriga (Kenyon, Gómez & Whitney 2008; Kraus & Hillenbrand 2009; Torres et al. 2009; Kraus et al. 2017), in the literature without much information and/or contradicting physical parameters. We have focused only on objects classified as weak-line TTSs. In order to have sufficient SNR of obtained spectra, we have hand-picked stars with $V < 11$ mag, this is our observational limit (such star with $V = 11$ mag has SNR =15 in 15 min exposure). Here, we have aimed to refine their physical parameters. The same sample was used for spectroscopic follow-up observations at Stará Lesná, Skalnaté Pleso, and Tautenburg observatories.

The structure of the paper is the following: in Section 2 we describe the properties of detectors and the process of data acquisition and reduction. In Section 3.1, we present the technique used for radial velocities (RVs) determination and EW measurements. We deal with the proper atmospheric modelling in Section 3.3, where we also list our results. These are then used to refine the evolutionary status of observed objects in Section 4. The discussion and physical characteristics of all targets are included in Sections 5 and 6.

Table 2. Overview of the spectroscopic material obtained. ASI spectra were not suitable for atmospheric modelling with `iSpec`. SLO data from 2022 were used only for RV measurements.

Site	R	Spectral range (Å)	Targets	Total spectra	Season
TLS	31 500	4590–7585	20	70	2017
SPO	38 000	4250–7320	4	4	2016–2018
SLO	11 000	4220–7078	21	80	2015–2017
			15	40	2022
ASI	1200	3300–7940	18	18	2018

2 OBSERVATIONS AND DATA REDUCTION

Spectroscopic observations of all selected targets were carried out with four different instruments (Table 2). We began at the Stará Lesná Observatory (SLO) in November 2015 with a 60-cm, f/12.5 Zeiss Cassegrain telescope equipped with a fibre-fed Echelle spectrograph

eShel (Pribulla et al. 2015). The spectra consisting of 24 orders cover the wavelength range from 4150 to 7600 Å. The resolving power of the spectrograph is about $R = 11\,000$. The Atik 460EX CCD camera, which has a 2749 × 2199 array chip, 4.54-μm square pixels, read-out noise of 5.1 e^- and gain 0.26 e^-/ADU, was used as a detector.

Since January 2016, we observed also at the Skalnaté Pleso Observatory (SPO), using the 1.3-m, f/8.36 Nasmyth-Cassegrain telescope equipped with a fibre-fed Echelle spectrograph of MUSICOS design (Baudrand & Bohm 1992). The spectra were recorded using an Andor iKon-L DZ936N-BV CCD camera with a 2048 × 2048 array, 13.5-μm square pixels, 2.9 e^- read-out noise and gain close to unity. The spectral range of the instrument is 4250–7375 Å (56 Echelle orders) with the maximum resolution of $R = 38\,000$ around λ 6000 Å.

The raw data from both SLO and SPO were reduced using `IRAF` package tasks, Linux shell scripts, and `FORTRAN` programs (Pribulla et al. 2015; Garai et al. 2017). In the first step, master dark and flat-field frames were produced. In the second step, the photometric calibration of the frames was done using dark and flat-field frames. Bad pixels were cleaned using a bad pixel mask, cosmic hits were removed using the program of Pych (2004). Typically three consecutive photometrically calibrated frames were combined to increase the signal-to-noise ratio (SNR) and clean the remaining cosmics. The Echelle order positions were defined by fitting the sixth order Chebyshev polynomials to a tungsten lamp and blue LED spectra tracings. In the next step, scattered light was modelled and subtracted. Aperture spectra were then extracted for both the object and the ThAr lamp frames and then the resulting 2D spectra were dispersion solved. The 2D spectra were finally combined into 1D spectra and rectified to the continuum.

In 2017, we obtained also spectra at Thüringen Landessternwarte (TLS) Tautenburg with the Alfred Jensch 2-m telescope and f/46 coudé Echelle spectrograph. These spectra cover 4510–7610 Å in 51 orders. A 2.2-arcsec slit was used for all observations giving $R = 31\,500$. For the wavelength calibration, we used a ThAr-lamp. The flat-fields were obtained using a screen in the dome and continuum lamps. Special care was taken that these lamps do not have the Li I 6708 emission line. Bias frames are obtained before the observations. Standard `IRAF` tools we used in order to subtract the bias, to flat-field the images, to remove the scattered light, to extract and wavelength-calibrate the spectra (see Hatzes et al. 2005; Guenther et al. 2009; Hartmann, Guenther & Hatzes 2010). The wavelength region used contains telluric lines that allow the removal of an instrument shift in wavelength.

On 2008 December 12, a collection of low-resolution spectra of 18 targets was obtained with the 1.22-m telescope operated in Asiago (ASI) by the Department of Physics and Astronomy of the University of Padova. The CCD camera is an ANDOR iDus DU440A with a back-illuminated E2V 42–10 sensor and 2048 × 512 array of 13.5-μm pixels. The whole optical train is highly efficient in the blue down to the atmospheric cut-off around 3200 Å. A 300-ln mm^{-1} grating blazed at 5000 Å provides a 2.31 Å pix^{-1} spectral dispersion, with spectra covering the ∼3300–8050 Å range. The slit width has been kept fixed at 2 arcsec (corresponding to a spectral resolution of 2.0 pix), and the slit (10-arcmin long) was always aligned with the parallactic angle for optimal absolute flux calibration. The observations of the targets were interspersed with those of nearby spectrophotometric calibrators selected from the internal Asiago data base. The spectra were reduced within `IRAF`, carefully involving all steps connected with correction for bias, dark and flat, sky subtraction, wavelength, and flux calibration.

3 SPECTRAL ANALYSIS

3.1 RV determination

To derive the RVs from the spectroscopic data we have used the broadening function (BF) technique (Rucinski 1992). BFs were extracted using a template depending on the spectral type of individual targets (Table 1).

For the BF extraction, we used only the green–yellow part of the spectrum from 4900 to 5500 Å, including the Mg I triplet (5165.8–5211.2 Å). This wavelength range is devoid of hydrogen Balmer lines, which are too broad to extract BFs, and there are no telluric lines affecting the results. On the other hand, for stars later than A the range contains numerous narrow metallic lines.

BFs were extracted with a step in RV of 10 km s^{-1} (SLO) or 3.5 km s^{-1} (SPO, TLS). Then the extracted BF profile was smoothed with a Gaussian function with $\sigma = 1.5$ of RV step. Projected rotational velocities, $v \sin i$, and RVs were determined by fitting a theoretical rotational profile to the smoothed BF. Linear limb-darkening law was assumed to keep the fitting function analytical (see Pribulla et al. 2014). The RVs derived from BFs were shifted to the IAU system (Evans 1967) using RVs of slowly rotating template stars (Seabroke et al. 2021), namely HD 03765 (K2V, $RV = -63.33 \pm 0.12$ km s^{-1}, $v \sin i = 5.29 \pm 1.34$ km s^{-1}), HD 23 169 (G2V, $RV = +14.57 \pm 0.14$ km s^{-1}, $v \sin i = 5.45 \pm 2.50$ km s^{-1}), and HD 65 583 (K0V, $RV = +14.79 \pm 0.12$ km s^{-1}, $v \sin i = 5.07 \pm 1.25$ km s^{-1}). The `vbroad` parameter from *Gaia* DR3 is fitted as due to axial rotation only (see Frémat et al. 2022), so we can adopt it as projected rotation velocity. The rotational broadening of the standard stars is well below the resolving power of the spectrograph used in this work (Table 2). The journal of spectroscopic observations including RV and $v \sin i$ measurements can be found in the appendix (Table B1). The measurement errors were derived from the covariance matrix of the least-squares optimization. For slowly rotating objects with $v \sin i \leq 20$ km s^{-1} the random errors are comparable to the spectrograph stability, which is at the level of 100–200 m s^{-1}.

The spectra of all target stars appear single-lined in our spectral resolutions. However, we list some peculiarities in Section 5. Our measured $v \sin i$ values are typically a few tens km s^{-1}. Considering that, there is a known sharp cut-off around 6400 K (e.g. Mallik, Parthasarathy & Pati 2003) for young dwarf and subgiants of spectral type F and G, our targets express higher rotation rates than expected (Fig. 1). Gallet & Bouvier (2015) developed angular momentum evolution models for low-mass stars, which account also for stellar-wind interactions that reproduce rotation behaviour between 1 Myr and 8–10 Gyr old stars. In our previous paper (Hambálek et al. 2019) we found periods of photometric variability, which we attributed to the rotation of a spotted surface. These periods fit nicely inside those modelled by Gallet & Bouvier (2015, fig. 5 therein) for young stars.

From measured RVs combined with parallaxes and mean proper motion from *Gaia* DR3, we used the `astropy` package to calculate space velocities U, V, and W and convert them to heliocentric using $[U_\odot = 11.1, W_\odot = 7.25]$ km s^{-1} (Schönrich, Binney & Dehnen 2010) and local Sun's galactic orbital velocity $\Theta_0 + V_\odot = 244$ km s^{-1}. The same procedure was repeated with RV values including the uncertainty for each target to derive the error. The results are presented in Table 3 and discussed in more detail in Section 5.

In addition, we have measured the EWs of H α, Li I 6104, and Li I 6708 lines (see a typical TLS spectrum in Fig. 2). The measurement was done using the standard task `splot` in the `IRAF` environment by marking continuum points on line ends and integrating over the line with interpolated continuum. We have also extracted the composite

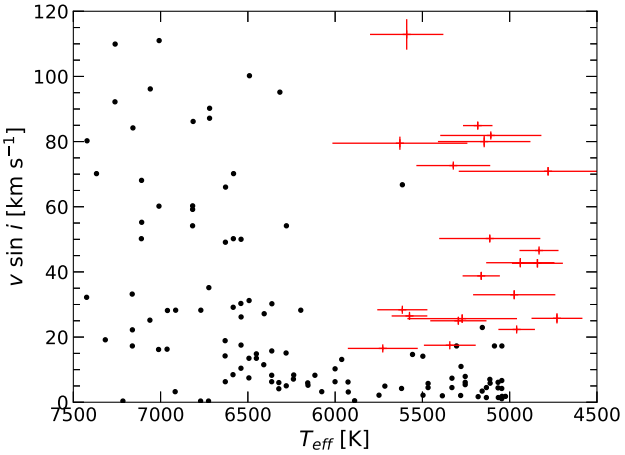

Figure 1. Dependence of the projected rotational velocity, $v \sin i$, on the effective temperature, $T_{\rm eff}$. Black points are data of MS stars from Mallik et al. (2003). Red error bars represent individual targets of this work. Results from `iSpec` modelling were used for the temperature. Rotation was measured using the BF method.

profiles of Na I D1 5896 and D2 5890 lines to measure the EWs of peaks of interstellar origin. See Section 3.4 for more details. Rough uncertainties were estimated according to the formula (Cayrel 1988):

$$\Delta EW \simeq \frac{\sqrt{FWHM \times p}}{SNR},$$

where *FWHM* and p are the FWHM of the Gaussian line profile and the width of the pixels in Å, respectively. All results from this section are presented in Table 3. We could not measure reliably the EW of H α line for HD 285281, HIP 20782, and HD 285 840 because of the strength of emission that was close to the total line itself and was barely distinguishable from the continuum. A similar problem was with sharp ISM lines of Na doublet that were not recognized in the available spectra due to SNR or spectral defects.

In the case of the Li I 6707.8Å line, there is a blend with Fe I 6707.41 line. Montes et al. (2001) did a study on several single stars of spectral types G-K, members of young (20 Myr and older) moving groups. They found the contribution of the Fe I line to be ~ 15 per cent of the total measured EW as a single profile. To quantify the strength of the iron line contamination, we can use an empirical relation $EW(\text{Fe } 6707.44) = 20 \times (B-V) - 3$ mÅ derived by Soderblom et al. (1993). The resulting EWs are listed in Table 3 in a column dubbed 'Fe 6707'. We note that in Table 3, the column 'Li 6708' is corrected for this value.

The other Li I 6104 is itself a triplet along with several lines of Fe, Ca blended over (see e.g. Ford, Jeffries & Smalley 2002). We did not have a sufficient spectral resolution to resolve individual parts and model them separately. For further results, we opted to use only the resonant line Li I 6708. We compare our measurements to the loci of Pleiades and other known TTS (in Covino et al. 2005) as well as potential post-TTS as defined by Martin (1997) in Fig. 3 using only the measurements of EW(Li 6708).

3.2 Spectral type determination

To derive the spectral type and luminosity class, the 3300–8000 Å spectra collected with the Asiago 1.22-m telescope on 18 of the program stars have been compared with the Asiago Spectral Library (ASL, Munari, in preparation), which covers the whole HR diagram (including chemically peculiar types like Carbon or S-type stars) with an instrument set-up identical to the one used in our observations. The spectral templates observed for inclusion in ASL were selected from the recommended lists of MK standard stars of Morgan & Keenan (1973, and references therein), Yamashita & Nariai (1977), Philip & Egret (1985, and references therein), Jaschek & Jaschek (1987), and Hoffleit & Warren (1995). The flux calibration is stable up to 0.05–0.08 mag as derived by inter-comparison of spectrophotometric standards observed along the program objects.

To compensate for uncertainties in flux calibration or differences in reddening, and so on, the spectra of program stars and of ASL templates were re-scaled by the localized geometric mean after being RV-shifted to null velocity. Prior to running a χ^2 fitting, the regions of the spectra affected by telluric absorption bands were masked. This mask weighs in the match results from individual lines and sub-parts of the spectrum. The χ^2 fitting was run in multiple modes, over the whole spectrum or just sub-sections, with or without masking the lines at risk of being affected by emissions or veiling (like Ca II H&K, Fe II, or the Balmer series), and so on.

This procedure robustly converged on the spectral type and luminosity class, and the results were all eye-checked for confirmation. A typical example of the resulting fit is presented in Fig. 4, where the target star HD 283782 is overplotted to the best matching ASL template (in this case the G2V star HD 126868). The two lower panels of Fig. 4 zoom on narrow spectral intervals around Ca II H&K and H β, to show how they are partially filled in by emission for program star HD 283782.

3.3 Atmospheric modelling of high-resolution spectra

Stellar atmospheric parameters were estimated using the `iSpec` software (Blanco-Cuaresma et al. 2014; Blanco-Cuaresma 2019). RVs were taken from Section 3.1.

We corrected spectra for barycentric RV. The system was checked again with respect to the telluric lines. The flux outside of the main absorption lines was normalized prior to the modelling. The region for fitting was selected as 4800–6800 Å, which contains Balmer lines sensitive to the temperature, Mg I triplet, Na I D lines sensitive to $\log g$ and various metallic lines. All targets exhibit rotationally broadened Na I lines (see $v \sin i$ in Table B1). Before the actual modelling of atmospheric parameters, we measured EWs of selected Balmer lines. Three targets (HD 283782, HD 283447, and HD 283518) show H α emissions. However, based on a comparison of target spectra to the Asiago spectral atlas, we find that all other targets have H α lines affected by emission to some extent. Thus, the region was excluded from further modelling.

The fitting consists of `iSpec` varying parameters and synthesizing spectra from the model library. We have used the default VALD line list (Kupka, Dubernet & VAMDC Collaboration 2011), which covers the optical and NIR region. The synthetic spectrum itself was generated with the `SPECTRUM` code by Gray & Corbally (1994) that uses Kurucz model atmospheres (Kurucz 2005). In Table 4, we list the parameter space used in this work. The synthetic spectra were convolved with a Gaussian function to correspond to the given spectral resolution. The projected rotational $v \sin i$ found from BF modelling was used to adjust the line width of model spectra.

The value of microturbulence (ξ) was kept free and the macroturbulence was automatically calculated by `iSpec`. We used a fixed value of the linear limb darkening coefficient (u).

The initial values of $T_{\rm eff}$ and $\log g$ were set from our previous photometry modelling (Hambálek et al. 2019). In several cases where no Strömgren photometry was available, we have applied random initial values for temperature and gravity inside the parameter space.

Table 3. Measured mean values of RVs, rotational line broadening, heliocentric velocities, and EWs of selected lines (in columns 8–13). In the case of sodium lines, only the interstellar absorption profile was measured. For HD 283447, the total EW of twin ISM peaks was used (see Fig. 5). Errors of individual parameters are in parentheses given by the least significant digit. Note: negative values of EW indicate lines found in emission.

TTS	Object name	RV [km s^{-1}]	$v \sin i$ [km s^{-1}]	U [km s^{-1}]	V [km s^{-1}]	W [km s^{-1}]	H α [mÅ]	Li 6104 [mÅ]	Li 6708 [mÅ]	Fe 6707 [mÅ]	Na 5890 [mÅ]	Na 5896 [mÅ]
01	HD 285281	+15.24(57)	80.50(67)	− 13.15(51)	− 5.78(7)	− 9.78(24)	–	370(21)	403(8)	20(2)	70(5)	73(5)
02	V1298 Tau	+14.42(34)	34.60(35)	− 12.61(31)	− 6.24(4)	− 9.18(13)	254(19)	383(20)	359(16)	17(2)	–	–
03	HD 284135	+14.99(41)	74.64(48)	− 13.66(38)	− 7.27(6)	− 9.57(15)	824(21)	243(15)	184(15)	9(1)	71(4)	74(4)
04	HD 284149	+15.49(29)	32.87(33)	− 13.93(26)	− 6.65(3)	− 8.97(11)	720(16)	222(13)	160(11)	9(1)	33(5)	13(5)
05	HD 281691	+10.51(22)	27.47(24)	− 13.00(21)	− 17.80(5)	− 8.01(6)	145(15)	369(17)	331(13)	13(2)	–	–
06	HD 284266	+15.61(41)	35.55(46)	− 13.66(38)	− 5.72(4)	− 9.61(15)	408(20)	295(18)	228(15)	11(3)	147(7)	30(7)
07	HIP 20782	+17.32(34)	52.19(40)	− 13.70(32)	− 8.30(1)	− 13.43(12)	–	238(18)	168(18)	4(1)	9(5)	4(5)
08	HD 284503	+14.47(47)	44.81(57)	− 15.49(45)	− 21.07(3)	− 3.49(15)	125(16)	306(15)	260(14)	14(2)	32(5)	20(4)
09	HD 284496	+15.60(35)	28.38(38)	− 13.66(33)	− 6.00(2)	− 9.97(11)	297(18)	345(18)	275(14)	13(2)	70(11)	31(11)
10	HD 285840	+22.23(49)	32.27(48)	− 19.80(46)	− 3.11(1)	− 10.96(16)	–	345(18)	214(14)	<1(3)	–	–
11	HD 285957	+17.61(48)	31.25(64)	− 15.48(45)	− 16.12(2)	− 7.41(17)	155(15)	377(18)	396(14)	15(4)	30(6)	52(6)
12	HD 283798	+13.82(28)	30.74(34)	− 12.64(27)	− 6.78(3)	− 10.69(6)	380(30)	305(13)	233(11)	10(1)	–	–
13	HD 283782	+16.78(66)	79.69(85)	− 16.39(64)	− 20.66(7)	− 15.10(14)	−3937(15)	245(19)	222(20)	15(1)	126(6)	117(6)
14	HD 30171	+18.64(1.44)	113.82(1.75)	− 16.71(1.36)	− 16.69(7)	− 6.28(46)	706(27)	269(23)	261(9)	12(1)	76(6)	68(6)
15	HD 31281	+15.00(48)	86.54(56)	− 12.44(46)	− 7.16(2)	− 10.32(13)	970(18)	233(15)	156(5)	11(1)	71(4)	68(4)
16	HD 286179	+13.56(24)	25.33(25)	− 11.31(23)	− 4.30(1)	− 8.07(8)	1316(17)	247(16)	158(11)	9(2)	–	–
17	HD 286178	+19.65(34)	46.63(37)	− 17.31(32)	− 16.86(3)	− 5.90(10)	211(17)	384(16)	401(15)	15(1)	51(6)	45(5)
18	HD 283447	+6.03(66)	52.42(71)	− 6.06(62)	− 12.67(13)	− 10.01(19)	−1397(22)	386(20)	475(18)	25(3)	108(11)∗	144(11)∗
19	HD 283572	+16.52(46)	81.60(51)	− 16.53(44)	− 12.00(8)	− 11.43(12)	899(15)	256(13)	262(14)	12(1)	82(3)	67(3)
20	HD 285778	+15.54(16)	21.52(17)	− 13.16(15)	− 6.28(1)	− 9.53(6)	510(18)	295(16)	255(11)	14(2)	–	–
21	HD 283518	+17.49(66)	74.75(80)	− 17.49(62)	− 11.26(12)	− 11.56(18)	−154(25)	394(26)	492(26)	25(5)	17(9)	9(9)

Note. ∗ = found a quadruple star, multiple absorptions in sodium profile, see text.

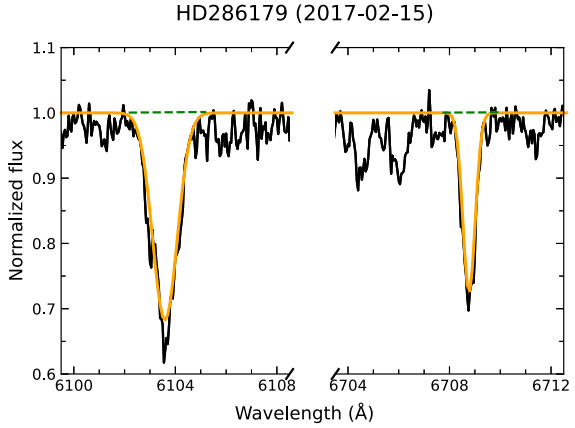

Figure 2. The region of Li I 6104 line (left-hand part) and Li I 6708 line (right-hand part) as measured for HD 286179 on 2017 February 15, at TLS (black). The range of EW measurement is shown as a green dashed line, while the Gaussian profile of the fit used for error estimates is overplotted as an orange solid line.

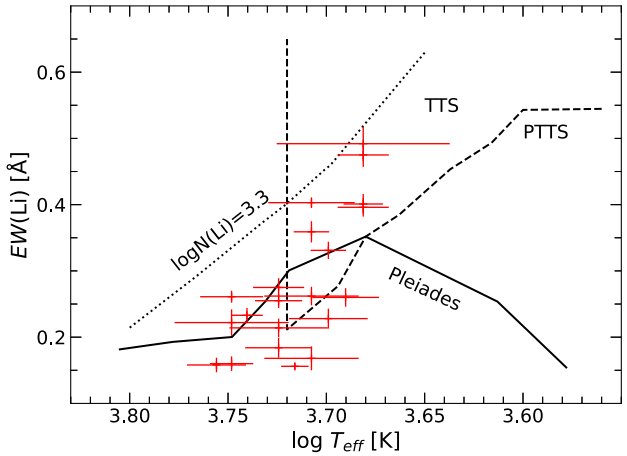

Figure 3. Measured EW of Li I 6708 line as a function of target star temperature as modelled by `iSpec`: Red error bars show individual targets. Underlying figure adopted from Covino et al. (2005), the boundary of post-TTS (PTTS, dashed line) taken from Martin (1997). The solid line shows the upper limit for the Pleiades cluster, while the dotted line indicates the cosmic abundance of lithium.

Because $T_{\rm eff}$, $\log g$, and [Fe/H] correlate, we have first modelled each spectrum with fixed [Fe/H] = 0. Afterward, the convergence was investigated in the $T_{\rm eff}-\log g$ plane. Initial values of temperature and gravity in various convergence runs were spread out evenly on a 3 by 3 grid in the parameter box. We have kept all results $T_{\rm eff}$, $\log g$, [Fe/H] along with their uncertainties. But we did not include an analysis of the exact abundances of individual species to further refine the metallicity.

Each converged model was saved with $T_{\rm eff}$, $\log g$ and their corresponding errors σ_T, σ_g calculated from standard deviation by `iSpec`. These values were used to construct a normalized bi-directional Gaussian distribution of results in the $T_{\rm eff}-\log g$ plane. See Appendix A1 for details. We derived two sets of error estimates: (i) finding the max value of probability in our model grid and applying the grid resolution, or (ii) treating the individual errors of $T_{\rm eff}$ and $\log g$ and constructing an arithmetic mean from all model results. In 2D plots in Appendix D, we have adopted the latter approach (as

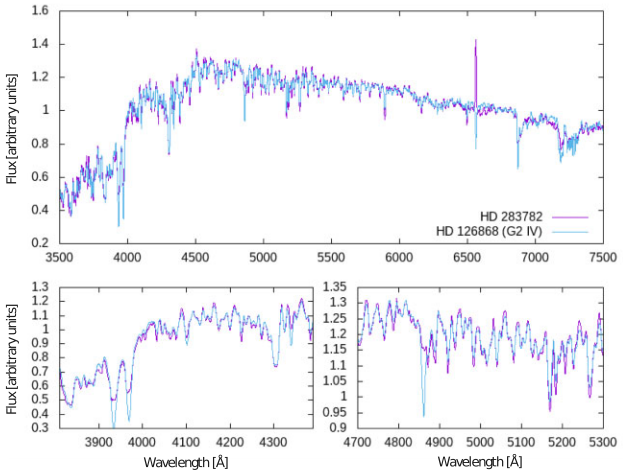

Figure 4. The object spectrum (HD 283782, TTS13, magenta) is overplotted to the best-fitting spectral template (blue) taken from the Asiago Spectral Atlas. The upper panel shows the whole spectrum while the lower two panels zoom on Ca II H & K lines (left-hand panel) and on H β regions (right-hand panel).

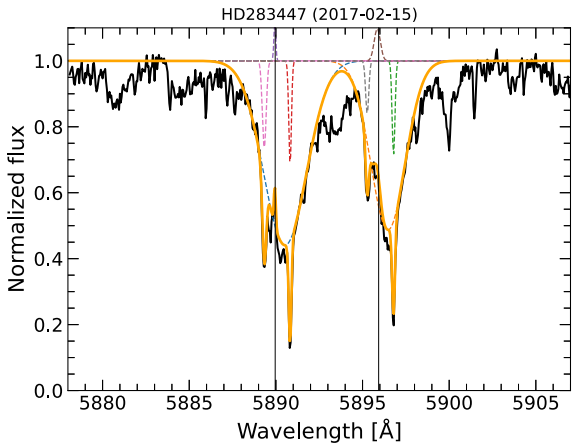

Figure 5. Sodium region of HD 283447 (TTS18) observed in TLS (black) with identified sharp ISM dips along with emissions from terrestrial lighting present on laboratory wavelengths (vertical lines). Total fit is superimposed as an orange thick line. Individual component profiles are displayed with coloured dashed lines.

Table 4. Range of parameters for atmospheric modelling. Single numbers represent the initial value. More information on fixed parameters is in the text.

Parameter	Range	
$T_{\rm eff}$ [K]	3500... 6000	
$\log g$	2.5... 5.0	
[Fe/H]	−1.0... +0.5	
[α/Fe]	0.0	Fixed
$v \sin i$ [km s^{-1}]	Adopted from BF	Fixed
ξ [km s^{-1}]	1.05	
u	0.6	Fixed
R	11 500, 31 500, 38 000	Fixed

displayed in the lower left corner). These errors are also presented in Table 5 under the iSpec modelling part.

Each numerical solution was visually checked for the fit of H β wings, Mg I triplet, and Na I lines. The next run was computed with new values of $T_{\rm eff}$, $\log g$, and [Fe/H] within respective ranges. The converged results are presented in Table 5 and the probability plots for individual stars in Figs D1–D4.

For comparison, we have included the astrophysical parameters from *Gaia* DR3 if available, also with reported errors. However, we must note a key difference. The RVS spectra used to infer $T_{\rm eff}$, $\log g$, and [Fe/H] in Gaia are based around the near-IR Ca II triplet (from 8470 to 8710 Å). This region contains also several weak lines of Si I, Ti I, Fe I (see Recio-Blanco et al. 2016). In our analysis, we have used a much broader spectral region, with mean resolving power comparable (∼11200 for RVS) or better (see Table 2). The present weak lines of neutral metals are not pressure sensitive and formed essentially in the same photometric layers as the continuum. The ratios of EWs of iron and vanadium lines (e.g. V I 6251.83Å to Fe I 6252.57 Å) are good temperature indicators for $T_{\rm eff} \geq 4000$ K (Gray 1994). Ratios of other lines such as Mg I triplet (5167.32–5183.60 Å), or Fe I 6042.2, 6056.0, 6200.3, 6219.3, 6703.6, 6705.1 Å combining with V I 6039.7, 6058.1, 6119.5, 6199.2 Å sensitive to temperature can be used (see e.g. Taguchi, Itoh & Mukai 2009). On the other hand, Ca I 6122.21, 6162.17, and 6439.08 Å have wings sensitive to gravity. We are confident that the spectrum fitted as a whole gives reasonable results. Unless stated explicitly, for further reference in this work, we are using only parameters and errors out of our iSpec analysis.

3.4 Temperature and reddening

We can also use the flux-calibrated spectra obtained in Asiago to roughly determine the temperature of the source. By comparing it to a library of synthetic spectra calibrated by fluxes computed out of photometry in various passbands. For this purpose, we used the BT-Settl model grid of theoretical spectra (Allard 2014) with Solar abundance (see e.g. Asplund et al. 2009). Models were confined to the same interval of temperatures and gravity as investigated with the iSpec code, namely $T_{\rm eff} \in [3500, 6000]$ K, $\log g \in [2.5, 5.0]$ with steps in 100 K and 0.5 dex, respectively. We have covered the spectral range of 3500–7900 Å.

The distance of Taurus–Auriga SFR is only around 140 pc (Kenyon, Dobrzycka & Hartmann 1994). All our targets are assumed to be disc-less WTTS. However, they are embedded in remnant dust and gas clouds. We can use the 3D dust map model Bayestar19 by Green et al. (2019) to estimate an upper limit of the reddening for a slightly larger distance in each line of sight. The model gives values of $E(g-r)$, which are recalculated[1] as $E(B-V) = 0.981 \times E(g-r)$.

We have used the distance D to individual targets from *Gaia* DR3 parallaxes (Gaia Collaboration et al. 2022). Star HD 284 135 (TTS03) has no measured parallax in *Gaia* DR3, so we assumed a mean distance of 140 pc. The Bayestar19 model gives also the statistical value of reliable distance modulus $\mu_r = 5\log_{10}(D_r) - 5$. However, in line of sight to our targets, there is a sparse population of stars with $\mu_r < 6$ (corresponding to ∼158.5 pc). For this reason, we can only estimate the upper value of the reddening derived from the Bayestar19 model.

We denote by D_0 the first bin in distance modulus with a non-zero value of $E(g-r)$ in the line of sight. This distance was compared to the distance of the target D as well as to the reliable distance for the model D_r. Usually $D < D_0 < D_r$, which means no effective reddening. The maximum value of $E(g-r)$ in the bin D_0 was then used to calculate the upper limit of $E(B-V)$. If a star had a distance $D > D_0$, we used the bin closest to the actual distance. One must be cautious since the typical reliable distance was $D_r \gtrsim 400 \pm 200$ pc. However, the mean distance with some reddening was found to be $D_0 = 158 \pm 40$ pc. The estimates are presented in Table 6 in column Bayestar19. Some evident discrepancies for individual targets are discussed further below.

Next, we probed our high-resolution spectra from TLS to find the intrinsic value of the reddening present. We have used the empirical relation by Poznanski, Prochaska & Bloom (2012) between the EW of Na I D absorption lines and $E(B-V)$. The errors were calculated by using the relation 9 from Poznanski et al. (2012) again with EWs adjusted by errors found earlier and reported in Table 3. We have identified the combined profile (see Fig. 5) of rotationally broadened stellar sodium lines D1 5896 and D2 5890 with potential sharp lines from the interstellar medium (ISM). In some cases there were blends, or no distinguishable ISM profile was found. EWs were measured only for the ISM part of the total profile. The results are listed in Table 6 in column four. The standard error of these $E(B-V)$ values is around 20 per cent.

Finally, we attempted to estimate the reddening from our Asiago flux-calibrated spectra. This was done by computing de-reddened spectra of objects using a range of typical values of $E(B-V)$ from 0.0 to 1.0 mag with a step of 0.05 mag. These were then compared with BT-Settl (Allard 2014) theoretical spectra. Model spectra were convolved with a Gaussian function to closely match the Asiago resolution. A running spline was constructed through continuum points for both the model and de-reddened spectra. We roughly estimate the value of $E(B-V)$ needed to fit the red continuum slope. The error is the step in our $E(B-V)$ range. The Asiago column in Table 6 contains these estimates. These values are larger which may result in higher temperatures.

4 ABSOLUTE PARAMETERS

To calculate luminosity, we used *Gaia* DR3 distances (d) (Gaia Collaboration et al. 2022) and found distance modulus $\mu = 5\log d - 5$. Then we can compute the absolute magnitude $M_V = V - \mu - A_V$, where $A_V = R_V \times E(B-V)$ and V is the magnitude from Table 1. $E(B-V)$ values are listed in Table 6 and $R_V = 3.1$. Utilizing bolometric corrections by Sung et al. (2013) or Eker et al. (2020) we can finally write $\log L = -0.4(M_V + \text{B.C.} - M_{\rm bol,\odot})$, where $M_{\rm bol,\odot} = +4.74$ mag, which corresponds to the nominal value for the Sun's luminosity (Prša et al. 2016).

The mean value of metallicity [Fe/H] for stars in our sample (see Table 5) is −0.38 dex and −0.381 dex from iSpec modelling and *Gaia* DR3 data base, respectively. The grid of models in masses and ages was spaced as follows:

$$\Delta M = \begin{cases} 0.05, & M < 1.0\,\mathrm{M}_\odot \\ 0.10, & M \geq 1.0\,\mathrm{M}_\odot \end{cases},$$

$$\Delta \text{age} = \begin{cases} 1, & \text{age} \leq 20\,\text{Myr} \\ 5, & \text{age} > 20\,\text{Myr} \end{cases}.$$

To estimate the masses and ages of our targets, we have used evolutionary tracks and isochrones of models with corresponding metallicity: [Fe/H] ∼ $\log(Z/X) - \log(Z_\odot/X_\odot)$. The Solar composition was set to $Z_\odot = 0.01377$, $Y_\odot = 0.2533$ as in Asplund, Grevesse & Sauval (2005). We used models pre-generated for deuterium frac-

[1] see http://argonaut.skymaps.info/usage

Table 5. Results of atmospheric modelling compared to earlier estimates from Strömgren photometry discussed in previous paper (Hambálek et al. 2019), best-fitting spectral template and *Gaia* DR3 solution. Corresponding T_{sp} for Asiago template spectra are taken from Sung et al. (2013).Errors of individual parameters are in parentheses given by the least significant digit.

		Strömgren photometry			Asiago		`iSpec` modelling			*Gaia* DR3 solution		
TTS	Object name	T_{eff} [K]	log g (cgs)	[Fe/H] [dex]	Sp. type	T_{sp} [K]	T_{eff} [K]	log g (cgs)	[Fe/H] [dex]	T_{eff} [K]	log g (cgs)	[Fe/H] [dex]
01	HD 285281	4817(557)	4.38(51)	−0.11	K0 V	5248	5146(310)	3.96(66)	−0.33(35)	6004(6)	3.897(8)	−0.789(57)
02	V1298 Tau	5171(151)	4.57(28)	+0.01	K1 V	5070	5163(244)	4.09(45)	+0.01(23)	4941(24)	4.227(9)	−0.340(29)
03	HD 284135	5700(236)	4.08(28)	−0.56	G2 V	5888	5323(359)	3.8(11)	−0.74(51)	–	–	–
04	HD 284149	6072(167)	4.16(31)	−0.65	F9 V	6089	5615(292)	4.06(54)	−0.65(56)	6105(8)	4.214(4)	−0.387(8)
05	HD 281691	5158(211)	4.61(26)	+0.19	K0 V	5248	4960(153)	4.10(25)	−0.46(23)	5035(23)	4.317(7)	−0.518(31)
06	HD 284266	5854(234)	4.38(39)	−0.13	G9 V	5404	4974(395)	3.90(70)	−0.77(41)	5246(39)	4.308(11)	−0.809(46)
07	HIP 20782	–	–	–	–	–	5114(342)	3.30(67)	−0.76(34)	–	–	–
08	HD 284503	5427(266)	4.15(39)	−0.23	G2 V	5888	4939(313)	3.78(67)	−0.48(23)	5801(4)	4.318(2)	−0.321(5)
09	HD 284496	5432(95)	4.43(66)	−0.23	G8 V	5559	5294(195)	4.33(41)	−0.19(30)	5143(11)	4.329(3)	−0.458(12)
10	HD 285840	5640(44)	4.45	–	–	–	5272(231)	4.36(38)	−0.30(32)	5386(7)	4.514(2)	−0.263(9)
11	HD 285957	4945(257)	4.79(25)	+0.06	–	–	4729(182)	3.97(31)	−0.78(24)	4959(14)	4.127(5)	−0.352(15)
12	HD 283798	5759(128)	4.69(36)	+0.60	G2 IV	5888	5574(310)	3.90(67)	−0.15(33)	5646(22)	4.279(3)	−0.375(22)
13	HD 283782	4937(660)	4.72(29)	+0.08	G2 IV	5888	5629(338)	3.69(90)	−0.30(64)	5753(6)	3.737(4)	−0.010(1)
14	HD 30171	5390(258)	4.04(51)	−0.35	G3 IV	5741	5590(471)	3.97(89)	−0.35(51)	–	–	–
15	HD 31281	5486(355)	3.97(48)	−0.56	G2 V	5888	5183(531)	3.7(11)	−0.79(51)	5766(13)	4.114(3)	−0.453(14)
16	HD 286179	5798(303)	4.63(44)	−0.15	G2 V	5888	5727(226)	4.40(67)	−0.16(22)	5842(6)	4.291(3)	−0.352(7)
17	HD 286178	4490(87)	4.64	–	K0 V	5248	4832(226)	3.92(62)	−0.40(30)	–	–	–
18	HD 283447	4049(55)	4.71	–	K2 V	4898	4841(265)	3.94(67)	−0.14(26)	–	–	–
19	HD 283572	5340(63)	4.51	–	G2 IV	5888	5108(387)	3.42(69)	−0.50(13)	5769(3)	3.936(1)	−0.205(3)
20	HD 285778	5304(254)	4.05(51)	−0.35	G7 V	5649	5343(212)	4.41(56)	−0.34(24)	5410(16)	4.271(3)	−0.394(17)
21	HD 283518	3770	4.78	–	K3 V	4732	4780(335)	3.68(41)	−0.38(39)	5353(33)	3.799(14)	−0.408(27)

Table 6. Comparison of different $E(B-V)$ in magnitudes estimated from dust map of Green et al. (2019) in column billed as Bayestar19, EW of Na I doublet (Sodium), and the red continuum slope from flux-calibrated spectra (Asiago). Details in text.

TTS	Object name	Bayestar19	Sodium	Asiago
01	HD 285281	<0.053	0.021(4)	0.25(5)
02	V1298 Tau	<0.168	–	0.15(5)
03	HD 284135	<0.027	0.021(4)	0.10(5)
04	HD 284149	<0.062	0.016(3)	0.10(5)
05	HD 281691	<0.194	–	0.15(5)
06	HD 284266	<0.009	0.023(4)	0.10(5)
07	HIP 20782	<0.009	0.015(3)	–
08	HD 284503	<0.009	0.016(3)	0.15(5)
09	HD 284496	<0.018	0.019(3)	0.15(5)
10	HD 285840	<0.009	–	–
11	HD 285957	<0.053	0.018(3)	–
12	HD 283798	<0.044	–	0.15(5)
13	HD 283782	<0.327	0.027(5)	0.40(5)
14	HD 30171	<0.062	0.021(4)	0.15(5)
15	HD 31281	<0.009	0.021(4)	0.10(5)
16	HD 286179	<0.009	–	0.15(5)
17	HD 286178	<0.009	0.018(3)	0.35(5)
18	HD 283447	<0.009	0.028(5)	0.60(5)
19	HD 283572	<0.009	0.021(4)	0.25(5)
20	HD 285778	<0.009	–	0.15(5)
21	HD 283518	<0.044	0.015(3)	0.30(5)

tional abundance $X_D = 4 \times 10^{-5}$ and mixing length parameter $\alpha = 1.68$.

The HR diagram was constructed using our `iSpec` temperatures and luminosities as calculated above. We find the probable mass by comparing the positions of our target stars to evolutionary tracks corresponding to the model with nearest [Fe/H] as determined by `iSpec`. The errors, mainly due to the effective temperature, but also in taking into account the uncertainty of `iSpec` result and model grid in [Fe/H], allow estimating the masses usually within $\pm 0.25\ \mathrm{M}_\odot$ (see Table 7).

We have found that all stars in our sample should be younger than 50 Myr. This is close, or inclusive, to the 10−100 Myr interval for the post-T-Tauri stars defined by Jensen (2001).

The age was estimated in a similar manner—comparing the loci of stars in the HR diagram with model isochrones. We have constructed the HR diagram for the appropriate Z, Y models for each target. However, for illustration purposes we plot them in Fig. 6 using the mean metallicity of the sample, i.e. we used the PMS evolutionary tracks and isochrones from Pisa Stellar Models (Tognelli, Prada Moroni & Degl'Innocenti 2011) for [$Z = 0.006$, $Y = 0.26$] which roughly corresponds to metallicity [Fe/H] ~ -0.36 dex.

We calculate the photometric radius from $(R/\mathrm{R}_\odot)^2 = L/\mathrm{L}_\odot \times (5777\ \mathrm{K}/T_{\rm eff})^4$ by using values for $T_{\rm eff}$ for different estimates out of Table 5.

To calculate the radius we use:

$$\log R(L,T) = \frac{1}{2}\left(\log\frac{L}{\mathrm{L}_\odot} - 4\log\frac{T_{\rm eff}}{T_{\rm eff,\odot}}\right). \quad (1)$$

This is further denoted by a subscript to indicate the source of $T_{\rm eff}$ value as follows: $R(L,T_i)$—`iSpec`, $R(L,T_A)$—Asiago, and $R(L,T_G)$—*Gaia*.

Alternatively, we can use $\log g$ (Table 5) and masses M (see Table 7, column 5) found from comparison with Pisa Stellar Models by Tognelli et al. (2011). Then using M, R in Solar units and comparing to the surface gravity of the Sun $\log g_\odot \sim 4.438$ (Prša et al. 2016), we can calculate the radius:

$$\log R(M,\log g) = \frac{1}{2}\left(\log\frac{M}{\mathrm{M}_\odot} - \log g + \log g_\odot\right). \quad (2)$$

In Table 7, we denote with a subscript i (`iSpec`) or G (*Gaia*) the source of $\log g$ value, while the mass is adopted from the target's position in HRD (according to the same-source temperature and absolute luminosity of a target).

An independent estimate of radii can be done from rotation rates ($P_{\rm rot}$) found in Hambálek et al. (2019) and the mean value of $v \sin i$ measured for every individual target in this work (see Table B1). The projected radius is then

$$R\sin i = \frac{P_{\rm rot}\, v \sin i}{2\pi \mathrm{R}_\odot}, \quad (3)$$

while keeping $P_{\rm rot}$ in seconds and the Sun's radius in kilometres. Any value $R(L,T) < R\sin i$ leads to contradiction $\sin i > 1$. Thus the projected $R\sin i$ is also the lower limit of stellar radius.

For example, in the case of HD 285281 (TTS01), we find that our `iSpec` estimates (subscript'i') of effective temperature $T_{\rm eff}$ differ from that reported in *Gaia* DR3 data (subscript 'G', see Table 5).

Finally, the projected (minimal) $R\sin i = 1.85\ \mathrm{R}_\odot$. Thus, radii $R(L,T_A)$ and $R(L,T_G)$ are not realistic. Our estimation of $T_{\rm eff}$ using `iSpec` gives a plausible value of R, with the inclination of rotational axis $i \sim 75$ deg. In Table 7, we print estimates of radii that are $<R\sin i$ including the uncertainty with *italics*.

5 SUMMARY AND DISCUSSION

5.1 Possible multiple systems

We have performed spectroscopic monitoring of targets previously selected and thought to be members of Taurus–Auriga SFR (Hambálek et al. 2019). We have measured the intrinsic radial and rotational velocities. Since we have gathered spectra in short bursts with gaps of hundreds of days, these are not usable for the investigation of radial–velocity curves.

For the majority of our targets, the RVs seem constant through the years 2016–2022, with the notable exception of HD 283447 (see Fig. C3). In our data, we have probably detected part of the RV curve of a binary. To investigate, we have used the broadened profile of Mg I triplet lines to find possible companions. A signal was detected (Fig. 7) in HD 283447 which is, within our detection limit, consistent with a four-component scenario presented by Duchêne et al. (2003). The two detected profiles are centred around RVs −8 and +58 km s^{-1} with rotational velocities 50 and 38 km s^{-1}, respectively. With our spectral resolution and sparse data, we cannot attribute these profiles to any component of the system.

Kenworthy et al. (2022) sketch the HD 283447 (V773 Tau) system with known binary Aa/Ab and possible hierarchical binary Ba/Bb with orbital periods of 51.1 and 63 d, respectively. Their outer orbit takes 26.5 yr for a full revolution. This means that the rotational profiles of A and B systems overlap in our total measured BF profile since both systems have their (absolute) respective barycentric RV $<<100$ km s^{-1}.

Also, the BF profile of HD 285281 was found to be strongly asymmetric. This could be caused by an unresolved companion, if we interpret the long wave in RV (Fig. C1) as an intrinsic signal, or more likely due to a large fraction of the spotted surface.

HD 30171 (TTS14) is another interesting object in terms of variable RV that seems to have an amplitude of the order of 10–

Table 7. Ages and masses from comparing positions in HR diagram to evolutionary PHOENIX models. Distances were set by *Gaia* DR3 parallaxes with reddening inferred from sodium measurement or from the 3D model Bayestar19 (see text). Projected radii calculated from $v\sin i$ and rotation rates from Hambálek et al. (2019). See details on $R(L, T)$ and $R(M, \log g)$ in text. Values of radii R typeset in *italics* are smaller than the minimal $R\sin i$ values. Errors of individual parameters are in parentheses given by the least significant digit.

TTS	Object	$\log T_i$	$\log L/L_\odot$	M [$M_\odot$]	age [Myr]	$R\sin i$ [$R_\odot$]	$R(L, T_i)$ [$R_\odot$]	$R(L, T_A)$ [$R_\odot$]	$R(L, T_G)$ [$R_\odot$]	$R(M, \log g_i)$ [$R_\odot$]	$R(M, \log g_G)$ [$R_\odot$]
01	HD 285281	3.711(25)	+0.43(1)	$1.45^{+0.10}_{-0.30}$	3^{+3}_{-2}	1.86(1)	1.92(38)	*1.51(18)*	*1.08(8)*	2.19(30)	2.36(6)
02	BD + 19656	3.713(20)	+0.07(2)	$1.25^{+0.10}_{-0.10}$	11^{+5}_{-4}	1.95(1)	*1.58(26)*	1.67(29)	1.82(34)	*1.67(14)*	*1.42(7)*
03	HD 284135	3.726(28)	+0.48(5)	$1.35^{+0.05}_{-0.30}$	2^{+2}_{-1}	1.21(1)	1.80(37)	1.67(27)	–	2.56(94)	–
04	HD 284149	3.749(22)	+0.28(5)	$1.20^{+0.10}_{-0.10}$	9^{+5}_{-3}	0.70(1)	1.16(15)	1.15(11)	1.15(10)	1.76(21)	1.47(9)
05	HD 281691	3.695(13)	−0.01(4)	$1.10^{+0.05}_{-0.05}$	8^{+2}_{-2}	1.43(1)	1.28(14)	*1.22(13)*	1.36(13)	1.61(5)	*1.26(4)*
06	HD 284266	3.697(33)	−0.01(9)	$0.95^{+0.05}_{-0.15}$	5^{+4}_{-3}	1.29(2)	*0.89(13)*	*1.08(8)*	*1.17(8)*	2.03(44)	1.27(9)
08	HD 284503	3.694(27)	+0.05(2)	$1.15^{+0.05}_{-0.20}$	5^{+4}_{-2}	0.65(1)	1.08(13)	0.88(6)	0.91(4)	2.43(42)	1.31(3)
09	HD 284496	3.724(19)	+0.00(3)	$1.05^{+0.05}_{-0.05}$	11^{+5}_{-4}	1.55(1)	*0.95(8)*	*0.89(6)*	*1.09(5)*	*1.19(9)*	*1.19(6)*
10	HD 285840	3.722(19)	−0.33(10)	$0.80^{+0.05}_{-0.05}$	28^{+12}_{-8}	0.99(1)	1.17(12)	1.40(15)	1.32(9)	1.01(9)	*0.84(3)*
11	HD 285957	3.675(16)	+0.12(13)	$0.75^{+0.20}_{-0.20}$	2^{+1}_{-1}	1.90(2)	*1.35(15)*	*1.54(18)*	*1.34(11)*	1.95(17)	*1.63(13)*
12	HD 283798	3.746(24)	+0.19(1)	$1.10^{+0.10}_{-0.10}$	12^{+5}_{-4}	0.60(1)	1.33(19)	1.26(13)	1.39(13)	2.03(39)	1.31(6)
13	HD 283782	3.750(25)	+0.96(18)	$2.10^{+0.35}_{-0.25}$	3^{+3}_{-2}	3.18(2)	3.28(1.94)	*2.04(63)*	*2.16(67)*	3.51(79)	3.32(24)
14	HD 30171	3.747(35)	+0.91(6)	$2.10^{+0.10}_{-0.50}$	3^{+4}_{-2}	2.49(3)	2.53(81)	2.15(55)	–	2.54(55)	–
15	HD 31281	3.715(42)	+0.54(5)	$1.20^{+0.25}_{-0.55}$	2^{+1}_{-1}	1.16(1)	1.95(49)	1.62(25)	1.71(25)	3.29(1.47)	1.97(26)
16	HD 286179	3.758(17)	+0.19(12)	$1.05^{+0.10}_{-0.10}$	15^{+7}_{-7}	1.56(1)	*0.93(8)*	*0.89(6)*	*0.91(4)*	*1.12(22)*	*1.27(6)*
17	HD 286178	3.684(20)	+0.18(7)	$1.15^{+0.15}_{-0.25}$	3^{+2}_{-1}	1.57(1)	2.39(63)	1.49(20)	–	2.15(34)	–
18	HD 283447	3.685(23)	+0.36(4)	$1.20^{+0.10}_{-0.30}$	2^{+1}_{-1}	3.19(5)	*2.51(53)*	*1.30(13)*	–	*2.17(42)*	–
19	HD 283572	3.708(32)	+0.53(4)	$1.55^{+0.10}_{-0.55}$	2^{+2}_{-1}	2.49(2)	2.30(71)	*1.78(33)*	*1.88(34)*	4.27(1.18)	2.36(23)
20	HD 285778	3.728(17)	+0.82(1)	$2.00^{+0.05}_{-0.30}$	2^{+1}_{-1}	1.21(1)	1.24(14)	*1.05(8)*	1.17(6)	1.53(16)	1.80(9)
21	HD 283518	3.679(29)	+0.14(4)	$1.15^{+0.10}_{-0.35}$	3^{+3}_{-1}	2.76(2)	*2.02(37)*	*1.49(17)*	*1.03(6)*	2.78(45)	*2.42(26)*

Note. HD 283447 (TTS 18) is modelled as a single star. However, $\log L/L_\odot$ is contaminated by third light in the system. The minimal radius $R\sin i$ is not affected.

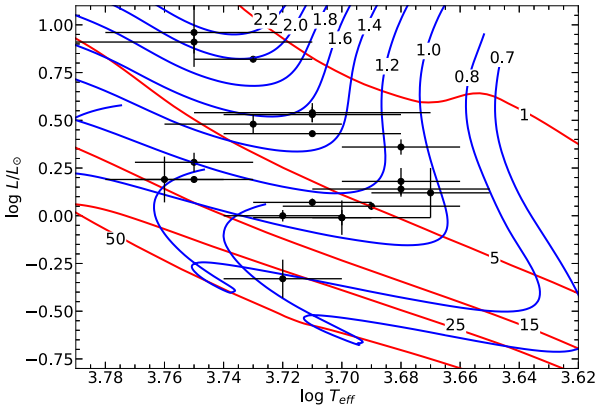

Figure 6. HR diagram for stars from Table 7. Blue solid lines show evolutionary tracks for stars of different solar masses (indicated by the number crossing a particular line), and red solid lines are isochrones for given age in Myr (indicated by a number crossing a particular isochrone). Evolutionary data from Pisa Stellar models (Tognelli et al. 2011) for [$Z = 0.006$, $Y = 0.26$] corresponding to the mean [Fe/H] ~ -0.36 of our sample for illustration.

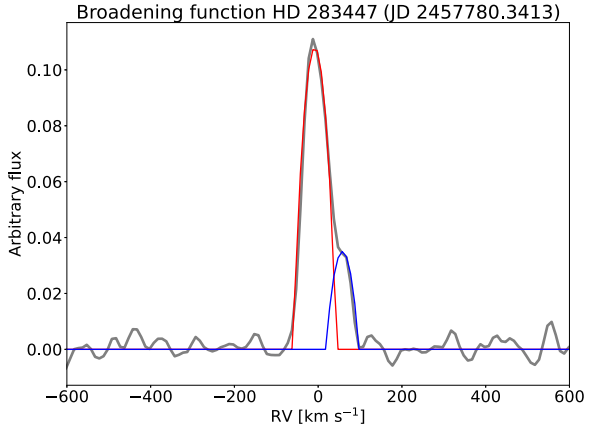

Figure 7. BF plot (grey) of HD 283447 from spectrum acquired on 2017 January 26 at SLO. Overplotted are two constituent rotational profiles (red and blue solid lines). Both of them are themselves unresolved close binaries.

20 km s^{-1} with a possible orbital period of roughly around 1.5–3 yr. Both of these objects warrant further observation.

In our subsequent analysis, we continued to work with HD 283447 as a single object, though age and mass are strongly affected by the third light of all components. However, we still could find a plausible solution for a single TTS with mass, radius, and temperature fitting the supposed class of object. This should serve as a cautionary case for future reference. This target is special in the sense that both constituent binaries are on similar orbits which produce non-detectable blends in spectral lines in lower-resolution spectrographs. A similar object is HD 283572 in terms of age, mass, and temperature (within errors), but bears no indication of RV changes (on a scale of days).

Based on RV measurements, HD 30171 appears to be another promising target. We observed gradual change of RV by $\sim$25 km s^{-1} in about 25 d from HJD 2457728.3152 (Fig. C3). This target is also a fast rotator with measured $v \sin i \sim 115$ km s^{-1}. We can compare this to the well-studied object HD 283518 (V410 Tau) that has a comparable $v \sin i \sim 71$ km s^{-1} and there is also a companion B, but on a 36-au orbit with 166-yr period (Yu et al. 2019). Thus the rapid rotation is not caused by close proximity of a companion star.

According to Bouvier et al. (1997), it is between 10 and 30 Myr that the moment of inertia of a solar-mass star decreases as the radiative core develops. We found that our targets HD 285281, HD 284135, HD 283782, HD 30171, HD 31281, HD 283447, HD 283572, and HD 283518 have ages $<5 \pm 3$ Myr and also $v \sin i > 70$ km s^{-1}.

5.2 Membership to Taurus–Auriga

The mean RV of targets was found between 10–20 km s^{-1}, which is consistent with other members of Taurus–Auriga SFR. Our individual targets were also a subset of the previous work of Kraus et al. (2017) and their measured RVs agree with our newer data.

We used *Gaia* DR3 proper motions and parallaxes and calculated the U, V, and W space–velocity components with our measured RV. For all targets, except the quadruple HD 283447, the results are in agreement with $U = -16.45 \pm 4.56$, $V = -13.08 \pm 2.52$, and $W = -10.97 \pm 4.04$ km s^{-1} as determined by Bertout & Genova (2006) or newer by e.g. Rivera et al. (2015).

Notably, the measured values of projected rotational velocity $v \sin i$ are higher than expected based on the rotation speed cut-off for temperatures lower 6400 K (Mallik et al. 2003) for young dwarfs and subgiants of spectral type F and G. In combination with measured EW of lithium and inferred ages from the HR diagram using model isochrones, this sits well with that our sample stars are in fact young and still rapidly rotating TTSs. Targets HD 284149, HD 284496, HD 285840, HD 283798, and HD 286179 exhibit a combination of age $>$ 10 Myr and $\log T_{\rm eff} > 3.72$. These could be candidates for post-TTSs as described by Jensen (2001).

We have compared our EW Li I 6708 measurements to those of White, Gabor & Hillenbrand (2007) and got values in agreement within reported errors, except for HD 31281 and HD 286179, which are in our case $\sim$5-times larger (see Fig. 2).

Soderblom et al. (1993) among other things investigated possible causes of variability of the EW of lithium resonance line. They report spectrum-to-spectrum rms in EW Li I 6708 only around 12 mÅ on a sample of K dwarfs from the Pleiades. They found no significant change no matter the time interval between observations. In early work (Soderblom 1989) also found no significant changes in overall colour with chromospheric activity, which implies that activity is unlikely to lead to variations in EW Li I 6708.

However, Soderblom et al. (1993) also modelled the effect of photospheric spots and temperature on the abundance of lithium. The cooler regions contribute less to the overall flux of a star, but the net value of EW Li will be larger. According to their result, almost any EW could be produced with sufficiently high spot coverage (up to 80 per cent). If the spots are distributed uniformly enough, no variability in EW Li will be observed.

5.3 Atmospheric parameters

In addition, we have also utilized Asiago spectral atlas to find the best-fitting templates to 18 targets (without HIP 20782, HD 285840, and HD 285957). These estimates agree with `iSpec` modelling in terms of effective temperature (spectral type). We have also checked *Gaia* DR3 solution, which shows higher values of $T_{\rm eff}$ for stars HD 285281 and HD 283518. We found these objects among stars with low age (of 5 ± 3 Myr). Atmospheric data from *Gaia* DR3 are also calculated using Ca II IR triplet. The Asiago spectra contained the Ca II H & K lines but they are not present in our high-resolution Echelle spectra. All targets show signs of emission in calcium (e.g.

in Fig. 4). This could affect $T_{\rm eff}$ determined by ESP-CS in *Gaia* DR3. According to Creevey et al. (2022), the ESP-CS pipeline uses Ca II IR triplet to compute stellar activity and compare it to the GSP_Phot routine when computing atmospheric parameters. The higher values of $T_{\rm eff}$ could be caused by Ca emission.

HD 283518 (V410 Tau) is a well-investigated star (see e.g. Stelzer et al. 2003; Grankin & Artemenko 2009). We find that the previous (Hambálek et al. 2019) estimate of effective temperature from Strömgren colour indices only was unrealistically low with only $T_{\rm eff} = 3770$ K. In spectra, H α was not very prominent with small emissions. H β and the rest of the Balmer lines were also affected and hard to locate. This could explain the higher measured value of $(b-y)$ that lead to underestimated $T_{\rm eff}$.

5.4 Impact of low metallicity

The majority of our targets display sub-solar metallicity [Fe/H] ranging from -0.79 to $+0.01$ dex with mean value -0.38 ± 0.32 dex. Alternatively, *Gaia* DR3 gives metallicity of our targets from the interval -0.8 to -0.01 dex (mean -0.38 ± 0.02). D'Orazi, Biazzo & Randich (2011) report [Fe/H] of Taurus–Auriga SFR as -0.01 ± 0.05 dex based on line modelling and veiling corrections. However, they have used only 7 K-type targets and only of spectral classes II and III, none of V, nor IV. If the modelled metallicity is indeed closer to solar, the inferred temperatures would be higher and consequently, masses corresponding to the given pair of $\log L/L_{\odot}$, $\log T_{\rm eff}$ would be higher by 12 per cent on average, depending on Z, Y of the model used. The solar-metallicity models also show ages of targets up to ∼50 per cent older.

5.5 Reddening

Our estimates of reddening based on sodium absorption give a mean value of $E(B-V) \sim 0.02$ mag with an error of 20 per cent. This is in good agreement with reddening based on 3D IR dust map (e.g. Green et al. 2019, Bayestar19) and leads to reliable luminosities. According to the dust-map model, HD 283782 has the highest $E(B-V)$ estimate of our targets. Rodriguez et al. (2017) have investigated this star because of two photometric dimmings of ∼0.12 mag found in data from years 2003 and 2009. They have concluded that it was caused possibly by a disc part or dust trap orbiting with $P > 13$ yr. This could be a reason for locally larger extinction.

The estimates of $E(B-V)$ using the slope of the red part of the continuum are an order of magnitude higher than other methods we used. However, this is not necessarily in contradiction, since the reddened slope may be caused solely due circumstellar matter or disc remnants. While the Bayestar19 values give values that are oriented in the direction of targets, the resolution of the dust map is between 3.4′ and 13.7′ (Green et al. 2019). Even in a short distance of <140 pc, it represents the stellar neighborhood. This value could be taken as a possible contaminant. Unfortunately, for the short distance, the actual sample of stars is too small, so only upper limits are somewhat reliable. Similarly, the estimation of $E(B-V)$ using the sodium doublet takes only the sharp ISM parts of the total profile into the account. On the other hand, the total reddening estimate from Asiago spectra takes into account the total spectral energy distribution (SED). The higher values could be attributed to matter in close stellar vicinity, e.g. remnants of protostellar disc filled with gas and dust.

If a target had a higher assumed temperature, i.e. earlier spectral type (as found from the Asiago catalogue), one would need generally higher $E(B-V)$ to fit the observed continuum slope.

In the case of HD 283447 (TTS18), the object with the largest $E(B-V)$, this is most likely the effect of a stellar component of late spectral type.

6 CONCLUSIONS

In continuation of our previous photometric study (Hambálek et al. 2019), we have performed the first high-dispersion spectroscopy and thorough spectral investigation on 21 selected weak-line TTSs. These targets had previously unknown or unreliable intrinsic parameters. Utilizing our own ground-based spectroscopic observations, we have gathered 212 spectra in total. Out of these, 154 were used to model atmospheric parameters (mainly $T_{\rm eff}$, $\log g$).

We have also investigated Na I lines, modelled their profile, and measured the EW of sharp absorption components of supposedly interstellar origin. We have used this as an independent proxy for estimating the extinction $E(B-V)$. This was used to correctly calculate luminosities based on available V magnitudes and *Gaia* DR3 distances.

We have measured the EW of Li I lines 6104 and 6708 to investigate their dependence on stellar temperatures inferred from spectral atmospheric modelling. Looking at Fig. 3, and considering errors, most of the targets fall in the area for much older Pleiades-like stars with only about seven falling in the T Tauri region, while there is none in the post-T Tauri locus. The fact that most of these objects are (∼100 Myr old) Pleiades-like from the lithium criterion is somewhat at odds with the estimated age <50 Myr from the derived stellar parameters (see Table 7) and by comparison with models on the HR diagram. Since the strength of the Li line may be affected by several processes (stellar magnetic activity, rotation, and so on), the lithium criterion should be considered only as a qualitative, not quantitative, indicator of youth (see e.g. Gutiérrez Albarrán et al. 2020).

We calculated absolute radii by using effective temperature acquired from atmospheric modelling and luminosity for updated distances from *Gaia* DR3 catalogue. We have compared these absolute radii to the projected (minimal) radius calculated from rotational rate $P_{\rm rot}$ found in our previous paper (Hambálek et al. 2019) with $v \sin i$ from this work.

We used PMS Pisa Models by Tognelli et al. (2011) to derive absolute mass and age estimates of targets. We found that all objects in our sample are younger than 50 Myr with mean age $\sim 5 \pm 3$ Myr and masses from the interval [0.75–2.10] $M_{\odot}$.

The evolutionary status of our targets was checked using accurate parallaxes from *Gaia* DR3 and mean stellar parameters. Based on lithium abundance, modelled age by location on the HR diagram, and large projected rotational velocities $v \sin i$, we can conclude that all our targets are young TTSs, some of them may be in the post-TTS stage. Still, the uncertainty of the effective temperature gives larger errors in estimating the age and mass.

We have used sparse RV measurements to explore potential companions to targets. Apart from already known quadruple HD 283447, we find an interesting object HD 30171, which would warrant follow-up observation. All other objects appear to be single. We have also calculated the spatial velocities U, V, and W of our targets, which are in agreement with mean values for Taurus–Auriga SFR.

ACKNOWLEDGEMENTS

This work was supported by the Slovak Research and Development Agency under the contract number APVV-20-0148. This work has also been supported by the VEGA grant of the Slovak Academy of Sciences number 2/0031/22. VK acknowledges the support from

the Government Office of the Slovak Republic within NextGenerationEU programme under project number 09I03-03-V01-00002. ZG furthermore acknowledges the support of the Hungarian National Research, Development and Innovation Office (NKFIH) grant K-125015, the PRODEX Experiment Agreement number 4000137122 between the ELTE Eötvös Loránd University and the European Space Agency (ESA-D/SCI-LE-2021-0025) and the support of the city of Szombathely. This work has made use of data from the European Space Agency (ESA) mission *Gaia* (https://www.cosmos.esa.int/gaia), processed by the *Gaia* Data Processing and Analysis Consortium (DPAC, https://www.cosmos.esa.int/web/gaia/dpac/consortium). Funding for the DPAC has been provided by national institutions, in particular, the institutions participating in the *Gaia* Multilateral Agreement.

DATA AVAILABILITY

Table B1 is available in a machine-readable format in the online supplementary material. If used, please cite this work as the source of the data.

REFERENCES

Allard F., 2014, in Booth M., Matthews B. C., Graham J. R., eds, Proc. International Astronomical Union. Vol. 299. Exploring the Formation and Evolution of Planetary Systems. Cambridge Univ. Press, Cambridge, p. 271
Asplund M., Grevesse N., Sauval A. J., 2005, in Barnes T. G., III, Bash F. N., eds, ASP Conf. Ser., Vol. 336, Cosmic Abundances as Records of Stellar Evolution and Nucleosynthesis. Astron. Soc. Pac., San Francisco, p. 25
Asplund M., Grevesse N., Sauval A. J., Scott P., 2009, ARA&A, 47, 481
Basri G., Batalha C., 1990, ApJ, 363, 654
Baudrand J., Bohm T., 1992, A&A, 259, 711
Bertout C., Genova F., 2006, A&A, 460, 499
Blanco-Cuaresma S., 2019, MNRAS, 486, 2075
Blanco-Cuaresma S., Soubiran C., Heiter U., Jofré P., 2014, A&A, 569, A111
Bonavita M., Daemgen S., Desidera S., Jayawardhana R., Janson M., Lafrenière D., 2014, ApJ, 791, L40
Bouvier J. et al., 1997, A&A, 318, 495
Campbell-White J. et al., 2023, A&A, 673, A80
Cayrel R., 1988, in Cayrel de Strobel G., Spite M., eds, Proc. International Astronomical Union, Vol. 132. The Impact of Very High S/N Spectroscopy on Stellar Physics. Springer, Berlin, p. 345
Covino E., Guenther E. W., Esposito M., Alcalá J. M., Frasca A., Mundt R., 2005, in Favata F., Hussain G. A. J., Battrick B., eds, ESA special publication, Vol. 560. Proc. 13th Cambridge Workshop on Cool Stars, Stellar Systems and the Sun. Springer, Berlin, p. 487
Creevey O. L. et al., 2022, A&A, 674, 35
D'Orazi V., Biazzo K., Randich S., 2011, A&A, 526, A103
Daemgen S., Bonavita M., Jayawardhana R., Lafrenière D., Janson M., 2015, ApJ, 799, 155
Duchêne G., Ghez A. M., McCabe C., Weinberger A. J., 2003, ApJ, 592, 288
Eker Z. et al., 2020, MNRAS, 496, 3887
Evans D. S., 1967, in Batten A. H., Heard J. F., eds, Proc. International Astronomical Union, Vol. 30. Determination of Radial Velocities and their Applications. Cambridge Univ. Press, Cambridge, p. 57
Feigelson E. D., Montmerle T., 1999, ARA&A, 37, 363
Fernández M. et al., 2004, A&A, 427, 263
Ford A., Jeffries R. D., Smalley B., 2002, A&A, 391, 253
Frémat Y. et al., 2022, A&A, 674, 19
Gaia Collaboration et al., 2022, A&A, 674, 22
Gallet F., Bouvier J., 2015, A&A, 577, A98
Garai Z. et al., 2017, Astronomische Nachrichten, 338, 35
Grankin K. N., 2013, Astron. Lett., 39, 251
Grankin K. N., Artemenko S. A., 2009, Inf. Bull. Var. Stars, 5907, 1
Grankin K. N., Artemenko S. A., Melnikov S. Y., 2007, Inf. Bull. Var. Stars, 5752, 1
Grankin K. N., Bouvier J., Herbst W., Melnikov S. Y., 2008, A&A, 479, 827
Gray D. F., 1994, PASP, 106, 1248
Gray R. O., Corbally C. J., 1994, AJ, 107, 742
Green G. M., Schlafly E., Zucker C., Speagle J. S., Finkbeiner D., 2019, ApJ, 887, 93
Guenther E. W., Hartmann M., Esposito M., Hatzes A. P., Cusano F., Gandolfi D., 2009, A&A, 507, 1659
Gutiérrez Albarrán M. L. et al., 2020, A&A, 643, A71
Hambálek L., Vaňko M., Paunzen E., Smalley B., 2019, MNRAS, 483, 1642
Hartigan P., Edwards S., Ghandour L., 1995, ApJ, 452, 736
Hartmann M., Guenther E. W., Hatzes A. P., 2010, ApJ, 717, 348
Hartmann L., Herczeg G., Calvet N., 2016, ARA&A, 54, 135
Hatzes A. P., Guenther E. W., Endl M., Cochran W. D., Döllinger M. P., Bedalov A., 2005, A&A, 437, 743
Herbig G. H., 1962, Adv. Astron. Astrophys., 1, 47
Hoffleit D., Warren W. H., Jr, 1995, VizieR Online Data Catalog. Université de Strasbourg, Strasbourg, p. V/50
Høg E. et al., 2000, A&A, 355, L27
Ingleby L. et al., 2011, ApJ, 743, 105
Jaschek C., Jaschek M., 1987, The Classification of Stars, 1st edn. Cambridge Univ. Press, Cambridge
Jensen E. L. N., 2001, in Jayawardhana R., Greene T., eds, ASP Conf. Ser., Vol. 244. Young Stars Near Earth: Progress and Prospects. Astron. Soc. Pac., San Francisco, p. 3
Kenworthy M. A. et al., 2022, A&A, 666, A61
Kenyon S. J., Dobrzycka D., Hartmann L., 1994, AJ, 108, 1872
Kenyon S. J., Gómez M., Whitney B. A., 2008, in Reipurth B., ed., Handbook of Star Forming Regions. Vol. 1 Astron. Soc. Pac., San Francisco, p. 405
Kraus A. L., Hillenbrand L. A., 2009, ApJ, 704, 531
Kraus A. L., Herczeg G. J., Rizzuto A. C., Mann A. W., Slesnick C. L., Carpenter J. M., Hillenbrand L. A., Mamajek E. E., 2017, ApJ, 838, 150
Kupka F., Dubernet M. L., VAMDC Collaboration 2011, Balt. Astron., 20, 503
Kurosawa R., Romanova M. M., Harries T. J., 2011, MNRAS, 416, 2623
Kurucz R. L., 2005, Memorie della Societa Astronomica Italiana Supplementi, 8, 14
Mallik S. V., Parthasarathy M., Pati A. K., 2003, A&A, 409, 251
Manzo-Martínez E. et al., 2020, ApJ, 893, 56
Martin E. L., 1997, A&A, 321, 492
Michalik D., Lindegren L., Hobbs D., 2015, A&A, 574, A115
Montes D., López-Santiago J., Fernández-Figueroa M. J., Gálvez M. C., 2001, A&A, 379, 976
Morgan W. W., Keenan P. C., 1973, ARA&A, 11, 29
Neuhaeuser R., Torres G., Sterzik M. F., Randich S., 1997, A&A, 325, 647
Neuhäuser R., 1997, Science, 276, 1363
Philip A. G. D., Egret D., 1985, in Hayes D. S., Pasinetti L. E., Philip A. G. D., eds, Proc. International Astronomical Union. Vol. 111. Calibration of Fundamental Stellar Quantities. Cambridge Univ. Press, Cambridge, p. 353
Poznanski D., Prochaska J. X., Bloom J. S., 2012, MNRAS, 426, 1465
Pribulla T. et al., 2014, MNRAS, 443, 2815
Pribulla T. et al., 2015, Astronomische Nachrichten, 336, 682
Prša A. et al., 2016, AJ, 152, 41
Pych W., 2004, PASP, 116, 148
Recio-Blanco A. et al., 2016, A&A, 585, A93
Rivera J. L., Loinard L., Dzib S. A., Ortiz-León G. N., Rodríguez L. F., Torres R. M., 2015, ApJ, 807, 119
Rodriguez J. E. et al., 2017, ApJ, 836, 209
Rucinski S. M., 1992, AJ, 104, 1968
Schönrich R., Binney J., Dehnen W., 2010, MNRAS, 403, 1829
Seabroke G. M. et al., 2021, A&A, 653, A160
Soderblom D. R., 1989, ApJ, 342, 823
Soderblom D. R., Jones B. F., Balachandran S., Stauffer J. R., Duncan D. K., Fedele S. B., Hudon J. D., 1993, AJ, 106, 1059
Stelzer B. et al., 2003, A&A, 411, 517

Sterzik M. F., Melo C. H. F., Tokovinin A. A., van der Bliek N., 2005, A&A, 434, 671
Sung H., Lim B., Bessell M. S., Kim J. S., Hur H., Chun M.-Y., Park B.-G., 2013, J. Kor. Astron. Soc., 46, 103
Symington N. H., Harries T. J., Kurosawa R., 2005, MNRAS, 356, 1489
Taguchi Y., Itoh Y., Mukai T., 2009, PASJ, 61, 251
Tognelli E., Prada Moroni P. G., Degl'Innocenti S., 2011, A&A, 533, A109
Torres R. M., Loinard L., Mioduszewski A. J., Rodríguez L. F., 2009, ApJ, 698, 242
Walter F. M., Alcala J. M., Neuhauser R., Sterzik M., Wolk S. J., 2000, in Mannings V., Boss A. P., Russell S. S., eds, Protostars and Planets IV. Univ. Arizona Press, Tucson, p. 273
Welty A. D., 1995, AJ, 110, 776
White R. J., Basri G., 2003, ApJ, 582, 1109
White R. J., Gabor J. M., Hillenbrand L. A., 2007, AJ, 133, 2524
Wichmann R. et al., 1996, A&A, 312, 439
Wichmann R. et al., 2000, A&A, 359, 181
Xing L. F., 2010, ApJ, 723, 1542
Xing L.-F., Li Y.-C., Chang L., Wang C.-J., Bai J.-M., 2021, A&A, 653, A28
Yamashita Y., Nariai K., 1977, An Atlas of Representative Stellar Spectra. Wiley, Hoboken
Yu L. et al., 2019, MNRAS, 489, 5556

SUPPORTING INFORMATION

Supplementary data are available at *MNRAS* online.

Appendix B. RV Measurements.
Appendix C. Radial Velocity Curves.
Appendix D. Probability Plots.

Please note: Oxford University Press is not responsible for the content or functionality of any supporting materials supplied by the authors. Any queries (other than missing material) should be directed to the corresponding author for the article.

APPENDIX: ADDITIONAL MATERIAL

A1 Convergence probability plots

We can investigate the convergence of `iSpec` fit procedure in the $T_{\rm eff}$−log g plane. Each resulting point (black dot in probability plots in Figs D1–D4) is obtained with errors in $T_{\rm eff}$ and log g values. We can treat these as σ-values for a bi-directional Gaussian function with components E_T and $E_{\log g}$:

$$E_T = \exp\left(-\frac{(T-T_0)^2}{2\sigma_T^2(1-C^2)}\right). \quad \text{(A1)}$$

$$E_{\log g} = \exp\left(-\frac{([\log g]-[\log g_0])^2}{2\sigma_g^2(1-C^2)}\right). \quad \text{(A2)}$$

Because the two variables are not independent, we must also include the cross-correlation term with a correlation coefficient C:

$$E_C = \exp\left(C\frac{(T-T_0)([\log g]-[\log g_0])}{\sigma_T\sigma_g(1-C^2)}\right). \quad \text{(A3)}$$

The final function is given as the product $A \times E_T \times E_{\log g} \times E_C$, where A is the normalization factor:

$$A = \frac{1}{2\pi\sigma_T\sigma_g\sqrt{1-C^2}}. \quad \text{(A4)}$$

We compute this component function for each pair of $[T_0, \log g_0]$ resulting from all `iSpec` model runs and then we sum all of them across the whole matrix of gridpoints $[T, \log g]$, $T \in [3500, 6000]$ K, $\log g \in [2.5, 5.5]$ dex to obtain the probability map.

We can then find two possible maxima: (i) from the peak position in the grid (upper left corner in probability plots, also noted with dashed-lined cross-hairs) with errors essentially determined by the coarseness of the grid, (ii) from the geometric mean of all model points and their σ errors (lower left corner in probability plots).

This paper has been typeset from a TEX/LATEX file prepared by the author.